Carbon 145 (2019) 195–200

Contents lists available at ScienceDirect

Carbon

journal homepage: www.elsevier.com/locate/carbon

Thermal conductivity of carbon nanotubes grown by catalyst-free chemical vapor deposition in nanopores

Evan Fleming [a], Feng Du [b], Eric Ou [a], Liming Dai [b], Li Shi [a, *]

[a] Department of Mechanical Engineering, The University of Texas at Austin, Austin, TX, 78712, USA
[b] Center of Advanced Science and Engineering for Carbon (Case4Carbon), Department of Macromolecular Science and Engineering, Case Western Reserve University, Cleveland, OH, 44106, USA

ARTICLE INFO

Article history:
Received 2 October 2018
Received in revised form
15 December 2018
Accepted 5 January 2019
Available online 7 January 2019

ABSTRACT

A graphitic structure was synthesized by catalyst-free chemical vapor deposition on an anodized aluminum oxide (AAO) template using acetylene as the carbon source at a temperature of 620 °C. The AAO template was removed by chemical etching, which yielded a three-dimensional structure featuring planar layers seamlessly joined together by nanotube pillars via continuous carbon-carbon bonding. Raman spectroscopy and transmission electron microscopy measurements reveal that the deposited carbon is nanocrystalline graphite with a thickness of about 10 nm. Carbon nanotubes were isolated from the three-dimensional nano-pillar graphitic structure and measured with a thermal four-probe method to obtain the intrinsic thermal conductance. Discrete modulated heating and Fourier transform analysis were used to improve the signal to noise ratio of the thermal measurement of the low-conductance nanostructure. The measured thermal conductivity of the nanotube wall increased with increasing temperature and was 3.9 ± 0.3 $Wm^{-1}K^{-1}$ at room temperature. Both the temperature dependence and the magnitude are consistent with the nanocrystalline graphitic structure.

1. Introduction

Low-dimensional carbon allotropes including two-dimensional (2D) graphene and one-dimensional (1D) carbon nanotubes (CNTs) have generated considerable interest for both basic studies of thermal physics and thermal management applications. Due to the elimination of interlayer van der Waals interaction, the basal plane thermal conductivity of freestanding graphene and CNTs can theoretically exceed that of highly-oriented pyrolytic graphite (HOPG) [1,2]. However, van der Waals interaction with a support, especially a support made of a dissimilar and defective structure, can reduce the thermal conductivity below the HOPG value [3]. Another limitation is that thermal transport is highly anisotropic in not only CNTs and graphene, but also in graphite, where the cross-plane thermal conductivity is two orders of magnitude lower than the basal plane value [4]. This limitation has motivated exploration of three-dimensional (3D) graphitic structures with isotropic thermal transport properties, which are desirable for most thermal management applications. Apart from graphitic foam structures previously investigated [5–9], a 3D continuous covalent structure consisting of planar graphene layers joined by vertical CNT pillars has been studied theoretically [10]. In addition to a number of theoretical calculations of the thermal transport properties of this 3D pillared graphene structure [10–13] and its epoxy composites [14], there have been theoretical studies of its mechanical properties [15] and its potential for use in hydrogen storage [16], gas separation and adsorption [17,18], and flexible super capacitors [19].

These theoretical studies have motivated experimental efforts to synthesize the 3D pillared graphene structure. In one experiment, a CNT forest connected to a graphene layer was grown by chemical vapor deposition (CVD) on a copper (Cu) thin film coated with several nanometer thick iron [20]. In another experiment, an additional alumina (Al_2O_3) layer was deposited on the iron (Fe) coated Cu growth substrate, which remained on top of the CNT arrays grown from the bottom graphene layer [21]. The difficulty in achieving C–C covalent bonding between a CNT and graphene layers on both ends of the CNT is due to the presence of the Fe catalysts for the CVD growth of high-quality CNTs [22]. In either the

* Corresponding author. University of Texas at Austin, Department of Mechanical Engineering, Austin, TX, 78712, USA.
E-mail addresses: eflem@utexas.edu (E. Fleming), fxd39@case.edu (F. Du), eric.ou@utexas.edu (E. Ou), lishi@mail.utexas.edu (L. Shi).

https://doi.org/10.1016/j.carbon.2019.01.023
0008-6223/

tip or base growth mechanism of the CNT, the Fe catalyst remains affixed to the CNT and prevents direct C–C bonding between the catalyst end of the CNT and a layer of graphene. The presence of catalyst at one end of the CNTs also prevents direct C–C bonding at both ends for vertical CNT arrays grown by a pyrolysis process between adjacent graphene layers in an expanded HOPG [23]. Meanwhile, a number of prior studies have reported the growth of large-diameter CNT arrays inside the nanopores of anodized aluminum oxide (AAO) templates with or without a catalyst [24–29]. Moreover, 3D graphitic structures have recently been grown on a tubular AAO template with a catalyst free CVD process [30], which used acetylene as the carbon source and the growth temperature of 620 °C is lower than those typically used for catalytic CVD growth of CNTs. The obtained CNT arrays are directly connected to two graphitic carbon layers at the top and bottom ends to form a 3D graphitic (3DG) structure.

The thermal transport properties of the CNT arrays and the 3DG structures grown in the AAO templates had not yet been characterized. The effective thermal conductivity in these 3DG materials depends on the geometric properties, including the pillar length and spacing, as well as the intrinsic solid thermal conductivity and quality of the deposited carbon layers. In particular, the effect of the relatively low growth temperature and the absence of a catalyst on the solid thermal conductivity of the deposited CNTs had not been studied.

Here, we report thermal transport measurements of the axial thermal conductance of individual CNTs isolated from a 3DG structure grown in an AAO template via the catalyst-free growth process. The thermal measurement is based on a recently reported four-probe thermal transport measurement method [31], which utilizes four suspended microfabricated metal line resistance thermometers to obtain both the intrinsic thermal conductance and the contact thermal resistance of a suspended nanostructure sample. For the measurement of the low-thermal conductance CNT sample, discrete modulated heating with Fourier transform analysis was employed to improve the signal to noise ratio. The obtained thermal conductivity increased with temperature and was 3.9 ± 0.3 $Wm^{-1}K^{-1}$ at room temperature for one sample. Both the temperature dependence and magnitude are consistent with the nanocrystalline graphitic structure observed by transmission electron microscopy (TEM) and Raman spectroscopy measurements. The observed low thermal conductivity suggests that the nanocrystalline porous graphitic materials is better suited for thermal insulation instead of heat spreading applications, in addition to potential applications for lithium ion batteries, where the nanocrystalline graphite was recently demonstrated to have improved cyclability over traditional graphite anodes [32].

2. Experimental methods

AAO templates purchased from ACS Material, LLC were used as the growth template. The AAO already had the aluminum film substrate removed and base pores opened to create open ends at both sides. The templates were placed in a 1 inch dimeter quartz tube furnace and heated to 620 °C under a mixture of argon and hydrogen at a flow rate of 200 sccm and 10 sccm, respectively. Once reaching the set temperature of 620 °C, acetylene was introduced at a flow rate of 20 sccm for 50 min, at which time the acetylene flow was stopped, and the furnace was cooled naturally. After growth, the AAO template was removed by etching in 5M NaOH for approximately 48 h. At this point the 3DG structure was rinsed in a series of deionized (DI) water and isopropanol (IPA) baths. A scanning electron microscopy (SEM) image of one 3DG sample, with a 2 μm thickness, is shown in Fig. 1 (a). The small pores (~100 nm) are visible in the planar surface. At the edge some of the CNTs fray away from the top carbon layer. The relatively large dark cracks on the bottom carbon layer are due to the etch process, as they were not visible prior to etching.

A typical Raman spectrum for the synthesized 3DG sample is shown in Fig. 1 (b). The presence of a D-peak at 1351 cm^{-1} and a separate G-peak at 1587 cm^{-1} and an intensity ratio, I(D)/I(G), of 0.89 indicates disordered nanocrystalline graphite [33,34]. This result is comparable to that reported for nanocrystalline graphite growth by molecular beam epitaxy at 600 °C on a sapphire substrate [35]. The I(D)/I(G) ratio can be used to evaluate the degree of nanocrystallinity. It has been suggested that the maximum theoretical I(D)/I(G) ratio of about 2.3 occurs at a uniform nanocrystalline grain size close to 2 nm [33]. This ratio decreases with both increasing grain size toward defect-free graphite and decreasing grain size toward amorphous carbon. The observed I(D)/I(G) ratio of 0.89 can occur when the grain size is either about 1 nm or 5 nm. In addition, the G peak increases slightly from 1581 cm^{-1} for perfect graphite to a maximum near 1600 cm^{-1} for nanocrystalline graphite, and decreases with further decreasing grain size to reach 1510 cm^{-1} for amorphous carbon [33]. The measured G-peak at 1587 cm^{-1} is close to the value for the maximum value for nanocrystalline graphite.

The intrinsic solid thermal conductivity of the nanocrystalline graphite plays an important role in the effective thermal conductivity of the 3DG structure. The solid thermal conductivity can vary

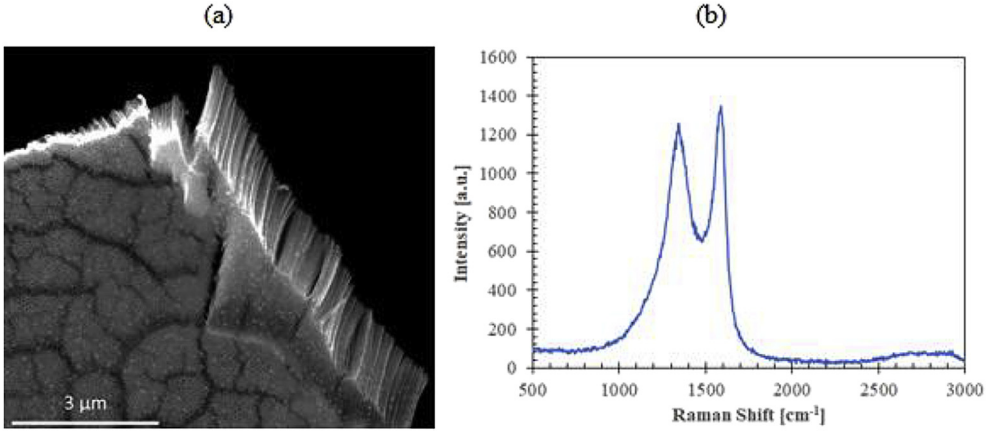

Fig. 1. (a) SEM image of the edge of a 3DG sample shown after template removal by NaOH. (b) Typical Raman spectra for the 3DG sample shows a D-peak centered at 1351 cm^{-1} and the G-peak at 1587 cm^{-1}. The laser wavelength is 488 nm. (A colour version of this figure can be viewed online.)

by four orders of magnitude during the transition from amorphous carbon to HOPG [4,36]. To evaluate the solid thermal conductivity of the nanocrystalline graphite synthesized by the catalyst free CVD process, we isolated individual CNTs from the 3DG structure and measured the solid thermal conductivity with the use of a four-probe thermal transport measurement method. In the sample preparation process, a single 3DG sample after AAO template removal was placed in IPA and sonicated to break up the structure into individual nanotubes, which were subsequently transferred to the four-probe device using a micro-manipulator under an optical microscope. Here we used AAO templates approximately 50 μm thick to provide sufficiently long CNTs for the measurement device. A low magnification SEM image of the device is shown in Fig. 2(a) and a higher magnification image of the measured sample on the device is shown in Fig. 2(b).

Due to the small size of the sample and the nanocrystalline nature of the CNT, the intrinsic thermal resistance (R_i) of the three suspended segments of the CNT sample is as large as the order of 10^9 K/W. In order to obtain measurable temperature rises in the j^{th} thermometer line adjacent to the i^{th} thermometer line that is electrically heated, the thermal resistance ($R_{b,j}$) of the thermometer line needs to be increased by increasing the length to match R_i. Due to processing limitation and increased radiation loss with increasing beam length, the total length of the thermometer line is 300 μm.

In order to measure the low-thermal conductance sample, the four-probe thermal measurement method described in a recent report [31] was modified in this work to increase the measurement sensitivity. In this modified method, the Joule heating current in the i^{th} line was discretely stepped to values that follow a sinusoidal function. Fast Fourier transform (FFT) data analysis was used to analyze the measured DC heating current (I_{DC}) and voltage drop (V_{DC}) in the heating line and the voltage drop (ΔV_{AC}) along each of the other thermometer lines with a small AC sensing current. The FFT amplitudes of the measured responses in V_{DC}, I_{DC}, and ΔV_{AC} were used to calculate the thermally induced resistance changes in each line, $\Delta R_{j,i}$, and the Joule heating in the i^{th} heated line, $Q_{IV,i}$ (Supplementary Information). Here, the subscript i denoting the heater line was varied from 1 through 4, and the subscript j representing the resistance measurement in the jth line also varied from 1 to 4. Via FFT data analysis, we obtained a 4×4 matrix of the $dR_{j,i}/dQ_{IV,i}$ slope values. By measuring the electrical resistance (R_j) of the j^{th} thermometer line as a function of the sample stage temperature at zero heating current in the heater line, we obtained the temperature coefficient of resistance, dR_j/dT, which are used to convert the $dR_{j,i}/dQ_{IV,i}$ values into $\frac{d\overline{\theta_{j,i}}}{dQ_{IV,i}}$, where $\overline{\theta_{j,i}}$ is the average temperature rise of the j^{th} thermometer line when the ith line is Joule heated. The FFT technique established in this work for resistance thermometry is able to considerably improve the signal to noise ratio. We note that the improvement observed in this work has motivated the use of a similar FFT technique for enhancing the signal-to-noise ratio of a recent Raman thermometry measurement [37].

We have also measured the background signal (Supplementary Information) caused by parasitic heat transfer between the heating line and the thermometer line due to radiation, residual gas molecules in the sample stage that was evacuated with the use of a turbomolecular pump, and conduction in the substrate. With the measured background level subtracted, the 4×4 matrix of background-corrected $\frac{d\overline{\theta_{j,i}}}{dQ_{IV,i}}$ data can be used to obtain the thermal resistances ($R_{b,j}$) of the four thermometer lines, the contact temperature rise ($\theta_{c,j,i}$) of each thermometer line, and the heat flow ($Q_{j,i}$) from the jth thermometer line into the sample [31].

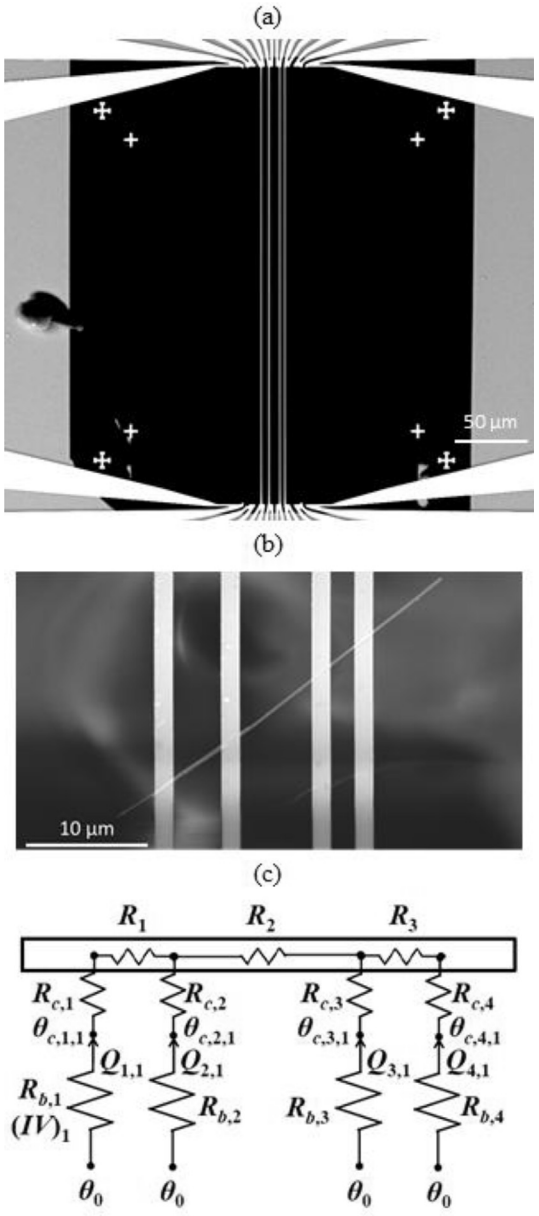

Fig. 2. (a) An SEM image of a four probe device without a sample. (b) SEM image of a CNT sample assembled on the four probe device. (c) A thermal circuit diagram of the four probe measurement device when line 1 is heated [31]. The rectangular box represents the sample and the three resistances (R_1, R_2, R_3) inside the box correspond to the intrinsic thermal resistances of the three suspended sample portions. $R_{c,j}$ is the contact resistances between the sample and the jth thermometer line. $R_{b,j}$ is the thermal resistance of the jth thermometer line. $Q_{j,i}$ and $\theta_{c,j,i}$ are the heat flow from the jth thermometer line into the sample and the jth thermometer line temperature rise at the contact to the sample when the ith line is heated. θ_0 is the substrate temperature rise, which is negligible.

The thermal circuit of Fig. 2(c) can be used to obtain the following set of eight equations

$$\theta_{c,1,i} - \theta_{c,4,i} = Q_{1,i}R_{1T} + (Q_{1,i} + Q_{2,i})R_2 - Q_{4,i}R_{4T} \quad (1)$$

$$\theta_{c,2,i} - \theta_{c,3i} = Q_{2,i}R_{c,2} + (Q_{1,i} + Q_{2,i})R_2 - Q_{3,i}R_{c,3} \quad (2)$$

where $R_{1T} \equiv R_{c,1} + R_1$, $R_{4T} \equiv R_{c,4} + R_3$, and i ranging from 1 to 4 represents the four different heating conditions. By casting these eight equations in the matrix form of $Ax = b$, we solved this over-

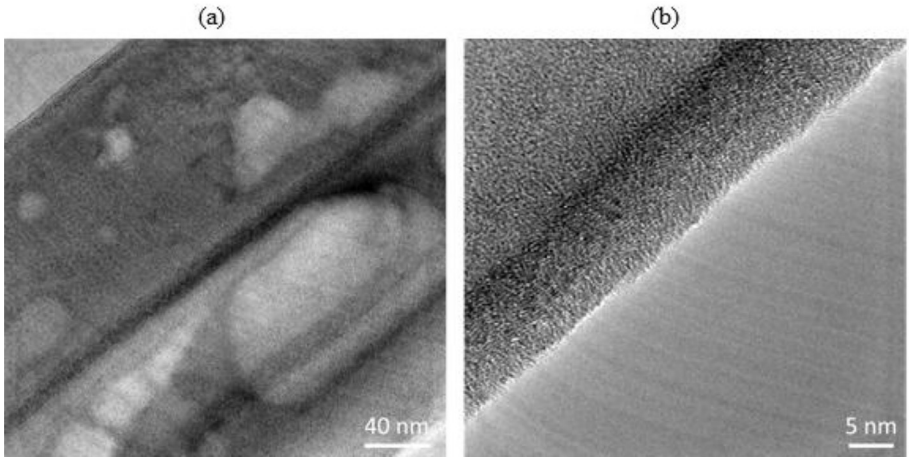

Fig. 3. (a) TEM image of the suspended portion of the sample between the two inner lines on the four probe device. (b) A higher magnification of one of the CNT walls.

determined system of equations using a least squares approach [38] given by $x = (A^TA)^{-1}A^Tb$ to obtain the five unknown resistances, R_{1T}, R_2, R_{4T}, $R_{c,2}$ and $R_{c,3}$. Here, R_2, the thermal resistance of the middle suspended sample segment, can be separately determined simultaneously from the two contact resistances of this segment, $R_{c,2}$ and $R_{c,3}$ because the heat flow rates in the three resistances are different. In comparison, the thermal resistances of the two end segments of the sample, R_1 and R_3, cannot be separated from the adjacent contact resistance, $R_{c,1}$ and $R_{c,4}$, because the heat flow through each end suspended segment is the same as that across the corresponding end contact.

The measured thermal conductance is converted to thermal conductivity based on the sample dimensions measured by SEM and transmission electron spectroscopy (TEM). As evident in the TEM image of the sample shown in Fig. 3(a), two tubes span the center gap of the four probe device. Fig. 3(a) also shows the presence of some voiding along the lengths of the tubes. The TEM image of Fig. 3 (b) shows there appears to be local ordering of the solid tube wall. This finding is consistent with the Raman spectrum that is characteristic of disordered nanocrystalline graphite. Although it is challenging to extract the exact grain size value from either the Raman and TEM measurements, both measurements suggest that the grain size is in the sub-10 nm scale. Based on the TEM measurements, the tube outer diameter is 98 ± 5 nm and the wall thickness is $10.5\ \text{nm} \pm 0.5\ \text{nm}$.

3. Results

The sample was measured in the temperature range between 100 K and 350 K at 50 K intervals. The measured thermal resistance of the sample is shown in Fig. 4, where the uncertainty was calculated by a Monte Carlo simulation based on the uncertainties in the measured $dR_{j,i}/dQ_{IV,i}$ and $(dR/dT)_{j,i}$ (Supplementary Information). The contact thermal resistance is much smaller than the sample thermal resistance of this sample with a large sample thermal resistance.

Using the geometry of the sample, the measured thermal resistance of the suspended sample in the center gap was converted to thermal conductivity. These data are shown in Fig. 5. Due to the presence of some voids on the nanotube wall, the reported thermal conductivities are expected to be slightly lower than the true intrinsic solid thermal conductivity of the catalyst-free, low temperature grown carbon. The room temperature thermal conductivity is $3.9 \pm 0.3\ \text{Wm}^{-1}\text{K}^{-1}$, which is a factor of about 500 lower

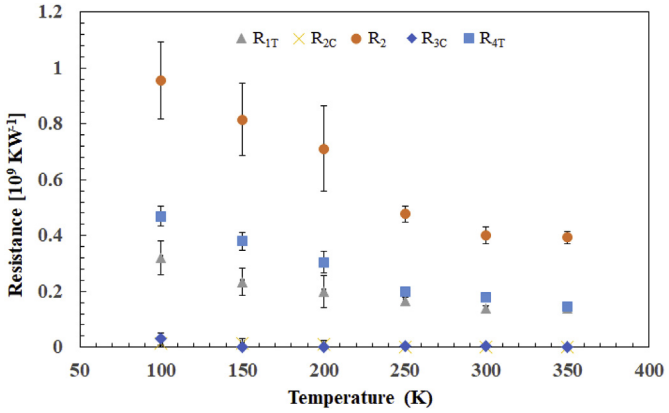

Fig. 4. Measured thermal resistances as a function of temperature. (A colour version of this figure can be viewed online.)

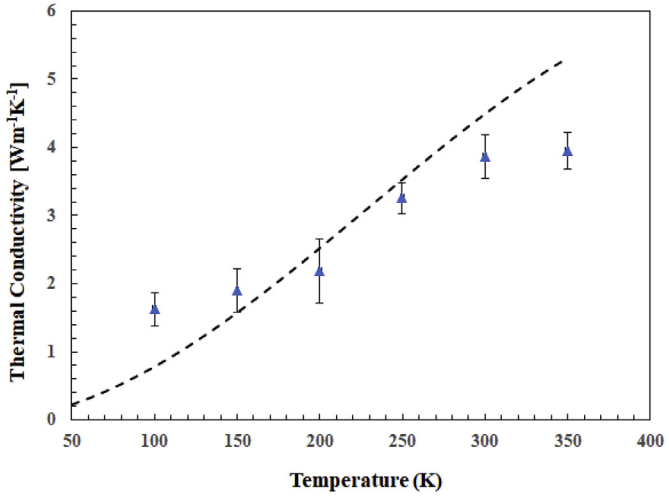

Fig. 5. Measured thermal conductivity for the CNT sample in comparison with the calculated thermal conductivity for a constant mean free path of 1.1 nm that is limited by grain boundary scattering in the nanocrystalline graphite. (A colour version of this figure can be viewed online.)

than the highest value reported for HOPG [3] and about 250 times lower than the highest reported values for catalytic CVD graphite foams [5].

Another indication of the defective graphite is that the peak thermal conductivity has not yet been reached at 350 K, which is far higher than that for highly oriented pyrolytic graphite, which peaks near 200 K. The shift of the peak temperature to a higher temperature indicates that defect and grain boundary phonon scattering processes dominate intrinsic umklapp phonon-phonon scattering even at room temperature. When the phonon mean free path is limited by grain boundary scattering to be the same as the grain size (d), the thermal conductivity is limited by the grain size as [39].

$$\kappa = \sum_{q} \hbar\omega v_x^2 \tau \frac{\partial f}{\partial T} \approx d \sum_{q} \hbar\omega \left| v_x \right| \frac{\partial f}{\partial T} \tag{3}$$

where the summation is over different phonon modes ($\boldsymbol{q}$), $\hbar$ is the reduced Planck's constant, v_x is the phonon group velocity component along the transport direction, τ is the phonon relaxation time, f is the Bose-Einstein distribution function, and T is the temperature. In comparison, the ballistic thermal conductance is calculated as [39].

$$G_{ballistic} = \sum_{v_x > 0} \hbar\omega v_x \frac{\partial f}{\partial T} \tag{4}$$

where the summation is over phonon modes with a positive v_x. Thus,

$$\kappa = 2dG_{ballistic} \tag{5}$$

Based on the reported ballistic thermal conductance data for graphite [40], we find that a grain size of 1.1 nm can reasonably fit the measurement results with Equation (5), as shown in Fig. 5. The more rapid increase of the calculated thermal conductivity with temperature than the measurement result can be attributed to the ignorance of umklapp phonon scattering in Equation (5).

4. Conclusions

Catalyst-free CVD growth on a highly ordered nano-porous AAO template yielded a graphitic structure featuring continuous C–C bonding between two planar layers bridged together by large diameter CNT pillars. The intrinsic graphitic quality obtained from this catalyst-free, low temperature CVD process has been characterized both structurally using Raman spectroscopy and TEM as well as thermally by measuring the thermal conductivity of individual CNT pillars. The structure and thermal characterization indicate that the catalyst-free CVD carbon is disordered nanocrystalline graphite with a room temperature solid thermal conductivity slightly higher than 3.9 ± 0.3 $Wm^{-1}K^{-1}$. The low thermal conductivity of the measured nanotubes led to the establishment of a highly sensitive measurement and data processing methodology for a previously reported four probe thermal transport measurement method [31]. Via spectral noise analysis using Fourier analysis, the thermal measurement sensitivity was considerably enhanced.

Acknowledgements

The experiments and the manuscript have been completed with support from Air Force Office of Scientific Research MURI award FA9550-12-1-0037. EO was supported by National Science Foundation (NSF) award CBET-1707080.

Appendix A. Supplementary data

Supplementary data to this article can be found online at https://doi.org/10.1016/j.carbon.2019.01.023.

References

[1] A.A. Balandin, Thermal properties of graphene and nanostructured carbon materials, Nat. Mater. 10 (2011) 569, https://doi.org/10.1038/nmat3064.
[2] M.M. Sadeghi, M.T. Pettes, L. Shi, Thermal transport in graphene, Solid State Commun. 152 (2012) 1321–1330, https://doi.org/10.1016/j.ssc.2012.04.022.
[3] J.H. Seol, I. Jo, A.L. Moore, L. Lindsay, Z.H. Aitken, M.T. Pettes, X. Li, Z. Yao, R. Huang, D. Broido, N. Mingo, R.S. Ruoff, L. Shi, Two-dimensional phonon transport in supported graphene, Science 328 (2010) 213–216, https://doi.org/10.1126/science.1184014.
[4] P.G. Klemens, D.F. Pedraza, Thermal conductivity of graphite in the basal plane, Carbon 32 (1994) 735–741, https://doi.org/10.1016/0008-6223(94)90096-5.
[5] M.T. Pettes, H. Ji, R.S. Ruoff, L. Shi, Thermal transport in three-dimensional foam architectures of few-layer graphene and ultrathin graphite, Nano Lett. 12 (2012) 2959–2964, https://doi.org/10.1021/nl300662q.
[6] I. Kholmanov, J. Kim, E. Ou, R.S. Ruoff, L. Shi, Continuous carbon nanotube-ultrathin graphite hybrid foams for increased thermal conductivity and suppressed subcooling in composite phase change materials, ACS Nano 9 (2015) 11699–11707, https://doi.org/10.1021/acsnano.5b02917.
[7] J.W. Klett, A.D. McMillan, N.C. Gallego, C.A. Walls, The role of structure on the thermal properties of graphitic foams, J. Mater. Sci. 39 (2004) 3659–3676, https://doi.org/10.1023/B:JMSC.0000030719.80262.f8.
[8] B. Hsia, M.S. Kim, L.E. Luna, N.R. Mair, Y. Kim, C. Carraro, R. Maboudian, Templated 3D ultrathin CVD graphite networks with controllable geometry: synthesis and application as supercapacitor electrodes, ACS Appl. Mater. Interfaces 6 (2014) 18413–18417, https://doi.org/10.1021/am504695t.
[9] Z. Chen, W. Ren, L. Gao, B. Liu, S. Pei, H.-M. Cheng, Three-dimensional flexible and conductive interconnected graphene networks grown by chemical vapour deposition, Nat. Mater. 10 (2011) 424–428, https://doi.org/10.1038/nmat3001.
[10] V. Varshney, S.S. Patnaik, A.K. Roy, G. Froudakis, B.L. Farmer, Modeling of thermal transport in pillared-graphene architectures, ACS Nano 4 (2010) 1153–1161, https://doi.org/10.1021/nn901341r.
[11] J. Shi, Y. Zhong, T.S. Fisher, X. Ruan, Decomposition of the thermal boundary resistance across carbon nanotube-graphene junctions to different mechanisms, ACS Appl. Mater. Interfaces 10 (2018) 15226–15231, https://doi.org/10.1021/acsami.8b00826.
[12] J. Park, V. Prakash, Phonon scattering and thermal conductivity of pillared graphene structures with carbon nanotube-graphene intramolecular junctions, J. Appl. Phys. 116 (2014), https://doi.org/10.1063/1.4885055.
[13] X. Yang, D. Yu, B. Cao, A.C. To, Ultrahigh thermal rectification in pillared graphene structure with carbon nanotube-graphene intramolecular junctions, ACS Appl. Mater. Interfaces 9 (2017) 29–35, https://doi.org/10.1021/acsami.6b12853.
[14] A. Lakshmanan, S. Srivastava, A. Ramazani, V. Sundararaghavan, Thermal conductivity of pillared graphene-epoxy nanocomposites using molecular dynamics, Appl. Phys. Lett. 112 (2018), https://doi.org/10.1063/1.5022755.
[15] L. Xu, N. Wei, Y. Zheng, Z. Fan, H.Q. Wang, J.C. Zheng, Graphene-nanotube 3D networks: intriguing thermal and mechanical properties, J. Mater. Chem. 22 (2012) 1435–1444, https://doi.org/10.1039/c1jm13799a.
[16] G.K. Dimitrakakis, E. Tylianakis, G.E. Froudakis, Pillared graphene: a new 3-D network nanostructure for enhanced hydrogen storage, Nano Lett. 8 (2008) 3166–3170, https://doi.org/10.1021/nl801417w.
[17] R.P. Wesołowski, A.P. Terzyk, Pillared graphene as a gas separation membrane, Phys. Chem. Chem. Phys. 13 (2011) 17027–17029, https://doi.org/10.1039/c1cp21590f.
[18] A. Pedrielli, S. Taioli, G. Garberoglio, N.M. Pugno, Gas adsorption and dynamics in pillared graphene frameworks, Microporous Mesoporous Mater. 257 (2018) 222–231, https://doi.org/10.1016/j.micromeso.2017.08.034.
[19] J. Lin, J. Zhong, D. Bao, J. Reiber-Kyle, W. Wang, Supercapacitors based on pillared graphene nanostructures, J. Nanosci. Nanotechnol. 12 (2012) 1770–1775, https://doi.org/10.1166/jnn.2012.5198.
[20] R.K. Paul, M. Ghazinejad, M. Penchev, J. Lin, M. Ozkan, C.S. Ozkan, Synthesis of a pillared graphene nanostructure: a counterpart of three-dimensional carbon architectures, Small 6 (2010) 2309–2313, https://doi.org/10.1002/smll.201000525.
[21] Y. Zhu, L. Li, C. Zhang, G. Casillas, Z. Sun, Z. Yan, G. Ruan, Z. Peng, A.R.O. Raji, C. Kittrell, R.H. Hauge, J.M. Tour, A seamless three-dimensional carbon nanotube graphene hybrid material, Nat. Commun. 3 (2012) 1225–1227, https://doi.org/10.1038/ncomms2234.
[22] J. Kong, A.M. Cassell, H. Dai, Chemical vapor deposition of methane for single-walled carbon nanotubes, Chem. Phys. Lett. 292 (1998) 567–574, https://doi.org/10.1016/S0009-2614(98)00745-3.
[23] F. Du, D. Yu, L. Dai, S. Ganguli, V. Varshney, A.K. Roy, Preparation of tunable 3D pillared carbon nanotube-graphene networks for high-performance capacitance, Chem. Mater. 23 (2011) 4810–4816, https://doi.org/10.1021/cm2021214.

[24] G. Meng, Y.J. Jung, A. Cao, R. Vajtai, P.M. Ajayan, Controlled fabrication of hierarchically branched nanopores, nanotubes, and nanowires, Proc. Natl. Acad. Sci. U.S.A. 102 (2005), https://doi.org/10.1073/pnas.0502098102, 7074–8.
[25] J.S. Suh, J.S. Lee, Highly ordered two-dimensional carbon nanotube arrays, Appl. Phys. Lett. 75 (1999) 2047–2049, https://doi.org/10.1063/1.124911.
[26] G. Che, B.B. Lakshmi, C.R. Martin, E.R. Fisher, R.S. Ruoff, Chemical vapor deposition based synthesis of carbon nanotubes and nanofibers using a template method, Chem. Mater. 10 (1998) 260–267, https://doi.org/10.1021/cm970412f.
[27] Y.C. Sui, D.R. Acosta, J.A. González-León, A. Bermúdez, J. Feuchtwanger, B.Z. Cui, J.O. Flores, J.M. Saniger, Structure, thermal stability, and deformation of multibranched carbon nanotubes synthesized by CVD in the AAO template, J. Phys. Chem. B 105 (2001) 1523–1527, https://doi.org/10.1021/jp002408o.
[28] N.M. Mohamed, M.I. Irshad, M.Z. Abdullah, M.S.M. Saheed, Novel growth of carbon nanotubes on nickel nanowires, Diam. Relat. Mater. 65 (2016) 59–64, https://doi.org/10.1016/j.diamond.2016.01.026.
[29] R. Wang, Y. Hao, Z. Wang, H. Gong, J.T.L. Thong, Large-diameter graphene nanotubes synthesized using Ni nanowire templates, Nano Lett. 10 (2010) 4844–4850, https://doi.org/10.1021/nl102445x.
[30] Y. Xue, Y. Ding, J. Niu, Z. Xia, A. Roy, H. Chen, J. Qu, Z.L. Wang, L. Dai, Rationally designed graphene-nanotube 3D architectures with a seamless nodal junction for efficient energy conversion and storage, Sci. Adv. 1 (2015) 1–10, https://doi.org/10.1126/sciadv.1400198.
[31] J. Kim, E. Ou, D.P. Sellan, L. Shi, A four-probe thermal transport measurement method for nanostructures, Rev. Sci. Instrum. 86 (2015), https://doi.org/10.1063/1.4916547.
[32] Z. Xing, Y. Qi, Z. Jian, X. Ji, Polynanocrystalline graphite: a new carbon anode with superior cycling performance for K-ion batteries, ACS Appl. Mater. Interfaces 9 (2017) 4343–4351, https://doi.org/10.1021/acsami.6b06767.
[33] A. Ferrari, J. Robertson, Interpretation of Raman spectra of disordered and amorphous carbon, Phys. Rev. B Condens. Matter 61 (2000) 14095–14107, https://doi.org/10.1103/PhysRevB.61.14095.
[34] A.C. Ferrari, Raman spectroscopy of graphene and graphite: disorder, electron-phonon coupling, doping and nonadiabatic effects, Solid State Commun. 143 (2007) 47–57, https://doi.org/10.1016/j.ssc.2007.03.052.
[35] S.K. Jerng, D.S. Yu, Y.S. Kim, J. Ryou, S. Hong, C. Kim, S. Yoon, D.K. Efetov, P. Kim, S.H. Chun, Nanocrystalline graphite growth on sapphire by carbon molecular beam epitaxy, J. Phys. Chem. C 115 (2011) 4491–4494, https://doi.org/10.1021/jp110650d.
[36] A.J. Bullen, K.E. O'Hara, D.G. Cahill, O. Monteiro, A. Von Keudell, Thermal conductivity of amorphous carbon thin films, J. Appl. Phys. 88 (2000) 6317–6320, https://doi.org/10.1063/1.1314301.
[37] F. Tian, B. Song, X. Chen, N.K. Ravichandran, Y. Lv, K. Chen, S. Sullivan, J. Kim, Y. Zhou, T.H. Liu, M. Goni, Z. Ding, J. Sun, G.A.G.U. Gamage, H. Sun, H. Ziyaee, S. Huyan, L. Deng, J. Zhou, A.J. Schmidt, S. Chen, C.W. Chu, P.Y. Huang, D. Broido, L. Shi, G. Chen, Z. Ren, Unusual high thermal conductivity in boron arsenide bulk crystals, Science 361 (2018) 582, https://doi.org/10.1126/science.aat7932.
[38] L.N. Trefethen, D. Bau III, Numerical linear algebra, Numer. Lin. Algebra Appl. 12 (1997) 361, https://doi.org/10.1137/1.9780898719574.
[39] G. Chen, Nanoscale energy transport and conversion, Nanoscale Energy Transp. Convers. (2005), https://doi.org/10.2221/jcsj.50.53.
[40] N. Mingo, D.A. Broido, Carbon nanotube ballistic thermal conductance and its limits, Phys. Rev. Lett. 95 (2005), 096105, https://doi.org/10.1103/PhysRevLett.95.096105.